Local pulsatile contractions are an intrinsic property of the myosin 2A motor in the cortical cytoskeleton of adherent cells

Michelle A. Baird[a], Neil Billington[a], Aibing Wang[b,c], Robert S. Adelstein[b], James R. Sellers[a], Robert S. Fischer[a], and Clare M. Waterman[a,*]

[a]Cell Biology and Physiology Center and [b]Genetics and Developmental Biology Center, National Heart, Lung and Blood Institute, National Institutes of Health, Bethesda, MD 20892; [c]College of Veterinary Medicine, Hunan Agricultural University, Changsha 410128, China

ABSTRACT **The role of nonmuscle myosin 2 (NM2) pulsatile dynamics in generating contractile forces required for developmental morphogenesis has been characterized, but whether these pulsatile contractions are an intrinsic property of all actomyosin networks is not known. Here we used live-cell fluorescence imaging to show that transient, local assembly of NM2A "pulses" occurs in the cortical cytoskeleton of single adherent cells of mesenchymal, epithelial, and sarcoma origin, independent of developmental signaling cues and cell–cell or cell–ECM interactions. We show that pulses in the cortical cytoskeleton require Rho-associated kinase– or myosin light chain kinase (MLCK) activity, increases in cytosolic calcium, and NM2 ATPase activity. Surprisingly, we find that cortical cytoskeleton pulses specifically require the head domain of NM2A, as they do not occur with either NM2B or a 2B-head-2A-tail chimera. Our results thus suggest that pulsatile contractions in the cortical cytoskeleton are an intrinsic property of the NM2A motor that may mediate its role in homeostatic maintenance of tension in the cortical cytoskeleton of adherent cells.**

Monitoring Editor
Yu-Li Wang
Carnegie Mellon University

Received: May 27, 2016
Revised: Nov 2, 2016
Accepted: Nov 18, 2016

INTRODUCTION

The spatial and temporal regulation of actomyosin cytoskeleton dynamics enables a variety of cell functions, including cytokinesis (Barr and Gruneberg, 2007; Zhou and Wang, 2008) and cell migration (Vicente-Manzanares *et al.*, 2009). In addition to these rapid cellular processes, which occur on the time scale of seconds or minutes, the actomyosin cytoskeleton is also responsible for driving large-scale changes in tissue architecture during developmental morphogenesis that are mediated by small changes in individual cell shape over much longer time scales. (Lecuit and Lenne, 2007). However, compared with what is known about the regulation of the cytoskeleton during rapid and dramatic changes in cell shape, much less is known about the underlying organization and dynamics of actomyosin during cellular mechanical homeostasis or slow processes such as morphogenesis.

Recent studies in model organisms have begun to shed light on the dynamics of the cytoskeleton during developmental morphogenesis. Several groups have shown that many types of tissue-level deformations are not driven by a continuous high rate of NM2 contractility in individual cells but are instead mediated by localized transient areas of contractile NM2 foci in the cortical cytoskeleton (Mason *et al.*, 2013) that we will refer to as "pulses." This was initially observed in *Caenorhabditis elegans* embryos (Munro *et al.*, 2004), where dynamic pulses of NM2 appear and disappear throughout the cortical cytoskeleton and transition to initiation of rapid directional cortical cytoskeletal flow, which drives zygotic polarization to set up the body axis of the future worm. This observation suggested that homeostatic maintenance of embryo shape may be sustained by a more dynamic cytoskeleton than previously thought.

This article was published online ahead of print in MBoC in Press (http://www.molbiolcell.org/cgi/doi/10.1091/mbc.E16-05-0335) on November 23, 2016.

*Address correspondence to: Clare M. Waterman (watermancm@nhlbi.nih.gov).

Abbreviations used: ECM, extracellular matrix; EM, electron microscopy; FWHM, full-width at half-maximal; GFP, green fluorescent protein; MEF, mouse embryonic fibroblast; MLCK, myosin light chain kinase; NM2, nonmuscle myosin 2; NM2A, nonmuscle myosin 2A; NM2A2b, nonmuscle myosin 2A nonmuscle myosin 2B chimera; NM2B, nonmuscle myosin 2B; NM2B2a, nonmuscle myosin 2B nonmuscle myosin2A chimera; NS, nonsignificant; RLC, regulatory light chain; ROI, region of interest; SERCA, sarco/endoplasmic reticulum calcium ATPase; siRNA, small interfering RNA; tdEos, tandem dimer Eos; TIRFM, total internal reflection fluorescence microscopy; WT, wild type.

Subsequently studies of NM2 dynamics in *Drosophila* revealed similar localized pulses of NM2 assembly/disassembly in the cortical cytoskeleton of epithelial cells in an array of developmental tissue movements and shape changes. These include development of the egg chamber during oogenesis (He *et al.*, 2010; Koride *et al.*, 2014), as well invagination, gastrulation, convergent extension, and organ remodeling in the embryo (Bertet *et al.*, 2004; Martin *et al.*, 2009; Mason *et al.*, 2013; Vasquez *et al.*, 2014; Munjal *et al.*, 2015). In epithelial cells in these tissues, transient appearance and disappearance of NM2 in the cortical cytoskeleton was shown to correlate with small changes in individual cell shape over time (Martin *et al.*, 2009; Solon *et al.*, 2009; Sokolow *et al.*, 2012; Mason *et al.*, 2013; Vasquez *et al.*, 2014). However, between individual cells within the epithelium, the pulses were asynchronous (Blanchard *et al.*, 2010; He *et al.*, 2010). A similar pulsatile behavior of actomyosin networks has also been observed during convergent extension in vertebrates (Skoglund *et al.*, 2008; Kim and Davidson, 2011). It is suggested that continuous contraction of epithelial cells in tissue could be unfavorable to tissue shape changes by either preventing directional movement of the tissue or promoting breakage of cell–cell junctions (Conti *et al.*, 2004; Rauzi *et al.*, 2010; Fernandez-Gonzalez and Zallen, 2011). To resolve this, it is believed that cells within a tissue use periodic and asynchronous contractile pulses, deforming cell shape without harming the tissue layer (Mason and Martin, 2011). Of interest, the durations of the pulses of NM2 observed in these diverse systems are similar, suggesting a common underlying mechanism.

What could regulate the pulsatile appearance and disappearance of NM2 foci in the cortical cytoskeleton? The active contractile form of NM2 is the bipolar filament, which is composed of ~30 NM2 molecules arranged with their motor domains at the ends and separated by a bare zone containing the rod domains and nonhelical tail pieces (Vicente-Manzanares *et al.*, 2009). Assembly of NM2 molecules into filaments is regulated by phosphorylation on various sites (Bresnick, 1999), and thus local kinase and phosphatase activity could mediate NM2 cortical cytoskeleton pulses. Furthermore, in higher vertebrates, there are multiple isoforms of NM2 that could modulate pulse activity. The two most widely expressed isoforms of NM2, A and B, can coassemble into filaments in cells, albeit in different ratios in different parts of the cell (Vicente-Manzanares *et al.*, 2008; Beach *et al.*, 2014). In addition, they differ significantly in the kinetics of their motor ATPase activity, with NM2A hydrolyzing ATP more rapidly and spending a larger fraction of its ATPase cycle dissociated from actin and NM2B spending more time actin-bound (Kovacs *et al.*, 2003; Rosenfeld *et al.*, 2003; Wang *et al.*, 2003; Vicente-Manzanares *et al.*, 2009). Thus regulation of NM2 pulses in the cortical cytoskeleton may be quite dynamic and multidimensional.

Here we sought to examine the dynamics of NM2 during homeostatic maintenance of tension in the cortical cytoskeleton of adherent cells in the absence of developmental signaling cues or cell–cell contacts. We combined live-cell imaging and quantitative analysis of green fluorescent protein (GFP)–tagged human NM2 isoforms in epithelial, mesenchymal, and bone-derived cells. We find that NM2A exhibits transient local accumulations in the basal cell cortical cytoskeleton that are mediated by local assembly and de novo formation of cytoskeletal networks. Not surprisingly, we show that pulses of local filament assembly require kinases involved in phosphorylation of the regulatory light chain, as well as increases in cytosolic calcium. However, surprisingly, we find that NM2 pulsing is specific to the NM2A isoform and is not observed for NM2B. Using pharmacological inhibition of ATPase activity, domain-swapped NM2A and NM2B chimeric constructs, and cells lacking endogenous NM2A, we show that the motor activity of NM2A is specifically required for NM2 pulsing in the cortical cytoskeleton. With these data, we suggest that the pulsatile assembly and disassembly of NM2A foci is an inherent property of cortical actomyosin networks in adherent cells at steady state and that pulse assembly and turnover are driven by the unique kinetics of the NM2A motor domain.

RESULTS AND DISCUSSION

Localized pulses of NM2A assembly and disassembly occur in the cortical cytoskeleton of single adherent cells of multiple types

We sought to examine the steady-state behavior of NM2 in the cortical cytoskeleton to determine whether pulsatile contractions occur in individual cells in isolation from developmental signaling cues and neighboring cells and dissect the mechanism of pulse regulation. To characterize the dynamic behavior of NM2, we tagged the N-terminus of full-length human NM2A with monomeric Emerald fluorescent protein (mEmerald-NM2A) and expressed it in adherent mesenchymal (primary mouse fibroblasts [MEFs]), epithelial (human breast adenocarcinoma [MCF-7]), or bone (human osteosarcoma [U2OS])–derived cells plated on 10 µg/ml fibronectin. mEmerald-NM2A correctly incorporated into stress fibers and peripheral arcs of the cytoskeleton in all three cell types (Figure 1, A–C). Using time-lapse total internal reflection fluorescence microscopy (TIRFM), we imaged mEmerald-NM2A dynamics in the ventral cortical cytoskeleton of U2OS cells over 30 min at 10-s intervals. Kymographs taken over the course of a single movie revealed the formation and dissolution of NM2A foci in different subcellular regions independently, out of synchrony, and with no apparent repeating frequency (Figure 1B). Line scans on individual NM2A punctae within these regions showed that NM2A often formed doublets of intensity separated by approximately the microscope resolution limit that are consistent in size and shape to NM2A filaments (Billington *et al.*, 2013; Beach *et al.*, 2014; Burnette *et al.*, 2014; Shutova *et al.*, 2014), suggesting that pulses consist, as least in part, of NM2A filaments (Figure 1B). Examination of time-lapse movies of mEmerald-NM2A dynamics showed that all three cell types exhibited similar distinct subcellular regions of rapid increase and decay of mEmerald-NM2A signal within the ventral cytoskeleton (Figure 1, B and C, and Supplemental Movie S1). We verified that local increases in mEmerald-NM2A fluorescence were due to an increase in molecular concentration as opposed to a TIRF artifact caused by transient local movement of the cortical cytoskeleton closer to the coverslip by coexpressing mEmerald-NM2A and a fluorescent membrane marker (mApple-CAAX). Analysis of dual-color TIRF movies showed that local increases in mEmerald-NM2A did not correspond to local increases in the mApple-CAAX signal (Figure 1D). Thus isolated cells of various types in tissue culture exhibit transient, local accumulations of NM2A in their ventral cortical cytoskeleton, similar to what has been observed in *C. elegans*, *Drosophila*, and *Xenopus* embryos (Munro *et al.*, 2004; Skoglund *et al.*, 2008; Martin *et al.*, 2009). We refer to these transient NM2A cortical cytoskeletal foci as "pulses."

We then sought to determine whether local NM2A pulses resulted from transport/motility of NM2A filaments from adjacent areas in the cortical cytoskeleton or were due to recruitment/assembly of NM2A in the local region. Kymograph analysis of time-lapse image series of mEmerald-NM2A in regions of pulses in U2OS cells failed to show long-range directional motion of mEmerald-NM2A puncta into or out of pulse areas from adjacent regions. However, small movement at variable directions and speeds was detected, including some short-range centripetal motion within pulses, possibly

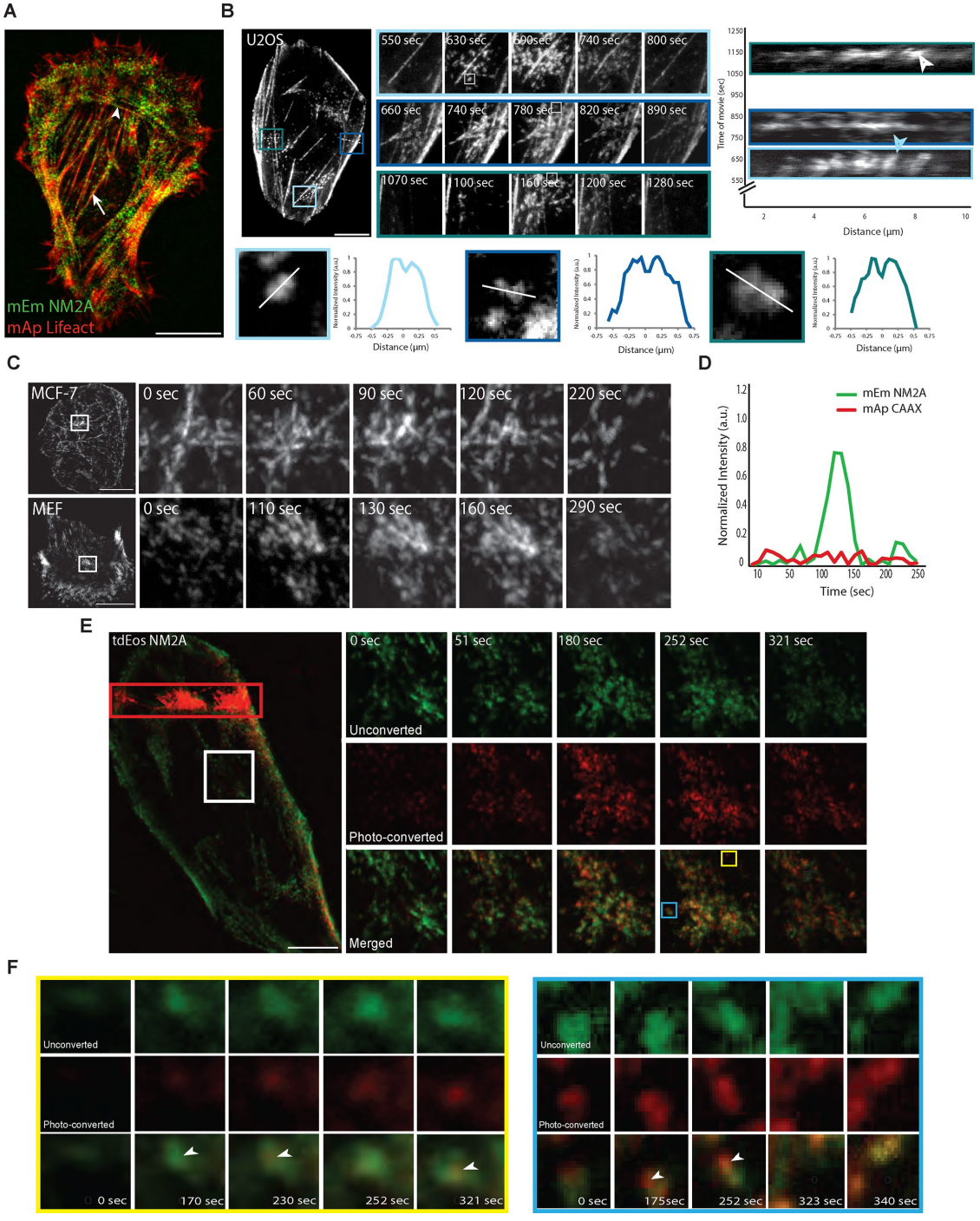

FIGURE 1: NM2A exhibits localized areas of pulsatile assembly and disassembly in the ventral cortex of adherent cells. (A) Human osteosarcoma (U2OS) cells plated on fibronectin-coated coverslips expressing mEmerald-NM2A (green) and mApple-Lifeact (red) and imaged live by TIRFM (evanescent field depth, 100 nm). White arrowhead indicates incorporation of NM2A into actin arcs, and white arrow indicates NM2A incorporation into stress fibers. (B) U2OS cell plated on fibronectin-coated coverslips expressing mEmerald-NM2A (top right). Boxes indicate regions of NM2A pulses that are shown as zoomed time-lapse image series (middle); white dotted line (=10 μm) indicates location of kymographs (right); white box indicates location of filaments subjected to line scans (white lines, bottom). Blue arrowhead indicates a NM2A punctae that was present at the start of the pulse that increased in intensity as the pulse grew; white arrowhead indicates the de novo formation of a new NM2A punctae within a forming pulse. Time shown indicates duration of movie (right). (C) Human breast adenocarcinoma (MCF7) and primary MEFs cells plated on fibronectin-coated coverslips expressing mEmerald-NM2A and imaged live by TIRFM. Boxed region (left) highlights individual NM2A pulses, shown zoomed in time-lapse image series (right); elapsed time in seconds with respect to the pulse. (D) Normalized intensity over time in the region of a NM2A pulse in a U2OS cell expressing mEmerald-NM2A and mApple-CAAX and imaged by TIRFM. (E) Time-lapse TIRFM of a U2OS cell expressing tdEos-NM2A (left); red box indicates photoconversion area; red and green represent photoconverted and unconverted tdEos, respectively. White

indicative of local contraction. Instead, kymographs showed that preexisting foci of mEmerald-NM2A fluorescence increased in intensity (Figure 1B, blue arrow), and new adjacent foci appeared and gained in intensity (Figure 1B, white arrow), followed by decrease in foci intensity and disappearance. To test more directly whether NM2A locally assembles at sites of pulses, we used the photoconvertible protein tdEos, to generate an NM2A fusion (tdEos-NM2A) to express in U2OS cells. We then photoconverted a region of tdEos-NM2A from green (unconverted) to red (photoconverted) in a nonpulsing region of the cell and tracked the increase in red fluorescence at a distal site in the NM2A network where a pulse was occurring (Figure 1, E and F, and Supplemental Movie S2). Examination of time-lapse movies showed that at the initiation of the pulse, only unconverted green punctae were present in the cortical cytoskeleton at the pulse site. However, as green NM2A fluorescence increased during pulse assembly, additional red photoconverted NM2A became incorporated into the pulse region. Close examination of dual-color movies revealed that during pulse assembly, individual green punctae present in the cortical cytoskeletal network before pulse initiation proceeded to incorporate red fluorescence as the pulse grew in size and intensity (Figure 1, E and F). In addition, some punctae appeared in the assembling pulse region de novo that incorporated both red and green NM2A (Figure 1F). These results indicate that formation of NM2A pulses is not driven by long-range contraction or motor-based transport of filaments from adjacent regions of the cortical cytoskeleton but by local recruitment of NM2A to the cortical cytoskeleton, which is assembled into both preexisting and newly formed NM2 structures.

Pulsatile dynamics of NM2A are stochastic but occur with a similar duration and frequency in multiple cell types

We next sought to characterize the kinetic properties of NM2A pulses in adherent cells. We quantified the fluorescence intensity in the regions of pulses over time in 30-min time-lapse TIRF movies of U2OS cells expressing mEmerald-NM2A. To standardize the classification of a cellular region as the site of a pulse, we used an automated image analysis algorithm designed for detecting pulses of cytoskeletal assembly in cells in *Xenopus* embryos (Kim and Davidson, 2011). This algorithm defined pulses as regions of interest (ROIs) in cells based on segmentation of spatially and temporally local fluorescence intensity increases and tracked changes in total intensity of each pulse ROI in the cell over time (Figure 2A). Plotting the fluorescence intensity in a pulse ROI from the beginning of the mEmerald-NM2A accumulation to the peak of the pulse to its dissipation to baseline level for many pulse events showed that the mean pulse assembly and disassembly rates were statistically indistinguishable from each other in U2OS, MEF, and MCF-7 cells (Figure 2B). The symmetry of the assembly and disassembly rates allowed us to fit a Gaussian model to the intensity versus time data from each pulse event and then define pulse duration as the full-width at half-maximum intensity (FWHM) of the Gaussian fit (Figure 2A). This analysis showed that pulse duration was not statistically different among the three cell types analyzed (Figure 2D). Fourier transform and power spectral analysis of pulse frequency failed to reveal any dominant periodicity (unpublished results). However, pulses occurred a similar number of times over the course of a 30-min movie in all three cell types (Figure 2C and Supplemental Movie S1). Comparison to previously documented cytoskeletal pulse durations showed that NM2A pulses in human and mouse cultured cells were similar in duration (within half an order of magnitude) to those observed in *Drosophila, Xenopus,* and *C. elegans* tissues in vivo (Figure 2E; Munro *et al.*, 2004; Martin *et al.*, 2009; Solon *et al.*, 2009; Fernandez-Gonzalez and Zallen, 2011; Kim and Davidson, 2011; Roh Johnson *et al.*, 2012). These data show that NM2A cortical cytoskeletal pulses occur stochastically but exhibit similar dynamics across a range of species and cell types.

NM2A pulses occur independently of integrin–ligand engagement but require intracellular or extracellular sources of calcium, regulatory light chain phosphorylation, and motor ATPase activity

We next focused on understanding what factors promote NM2A cortical cytoskeletal pulses. Previous studies showed that integrin-mediated cell–extracellular matrix (ECM) adhesion can regulate NM2 assembly and contraction (Klemke *et al.*, 1998; Polte *et al.*, 2004; Pasapera *et al.*, 2015). To test the hypothesis that NM2A pulses require integrin engagement to ECM, we plated U2OS cells expressing mEmerald-NM2A on poly-L-lysine–coated coverslips to mediate nonspecific adhesion. TIRF imaging and analysis showed that inhibition of integrin–ECM binding did not significantly affect mEmerald-NM2A pulse duration (59.31 ± 5.24 s) or frequency of occurrence (0.833 ± 0.065 pulses/30 min) compared with control cells plated on 10 µg/ml fibronectin (Figure 3, A and B, and Supplemental Movie S3). This suggests that integrin–ECM engagement is not required for NM2A pulsing in the cortical cytoskeleton.

We next addressed the role of calcium signaling in regulation of NM2A pulses. It is well established that calcium regulates myosin light chain kinase (MLCK)–mediated phosphorylation of NM2 regulatory light chain (RLC) and thus actomyosin contraction in cells (Hathaway and Adelstein, 1979). To reduce cytosolic calcium, we used gadolinium to inhibit extracellular calcium entry through stretch-activated channels in the plasma membrane (Yang and Sachs, 1989) or thapsigargin to inhibit calcium sequestration by the sarco/endoplasmic reticulum calcium ATPase (SERCA; Booth and Koch, 1989) and analyzed their effects on mEmerald-NM2A pulses in U2OS cells. Treatment with gadolinium (10 µM, 10 min) completely abolished mEmerald-NM2A pulses in the cortical cytoskeleton (Figure 3C). In addition, perfusion of gadolinium during time-lapse TIRF imaging caused immediate cessation and subsequent dissolution of existing pulses (unpublished data). Similarly, treatment of cells with thapsigargin (10 nM, 15 min) also dramatically reduced mEmerald-NM2A pulse frequency and duration (Figure 3, C and D, and Supplemental Movie S3). Thus, elevated cytosolic calcium from both stretch-activated channels and SERCA is required for the pulsatile dynamics of NM2A.

Because we found that calcium was required for NM2 pulsing in the cortical cytoskeleton and calcium regulates MLCK, we next addressed the role of phosphorylation of the RLC in NM2A pulsing. We treated cells with ML-7 (10 µM, 30 min) to inhibit MLCK (Saitoh *et al.*, 1987). Analysis of time-lapse movies showed that this caused

box highlights an individual pulse, shown zoomed in the time-lapse image series (right); elapsed time in seconds. Yellow and blue boxes highlight tdEos-NM2A filaments shown in F. (F) Zoomed time-lapse image series of the yellow and blue boxed regions in E; elapsed time in seconds. White arrows in yellow box indicate de novo appearance of a green unconverted tdEos-NM2A filament that subsequently incorporates red photoconverted tdEos-NM2A during a pulse. White arrows in blue box indicate de novo appearance of red photoconverted tdEos-NM2A in a previously green unconverted filament. Scale bar, 10 µm (A–C, E).

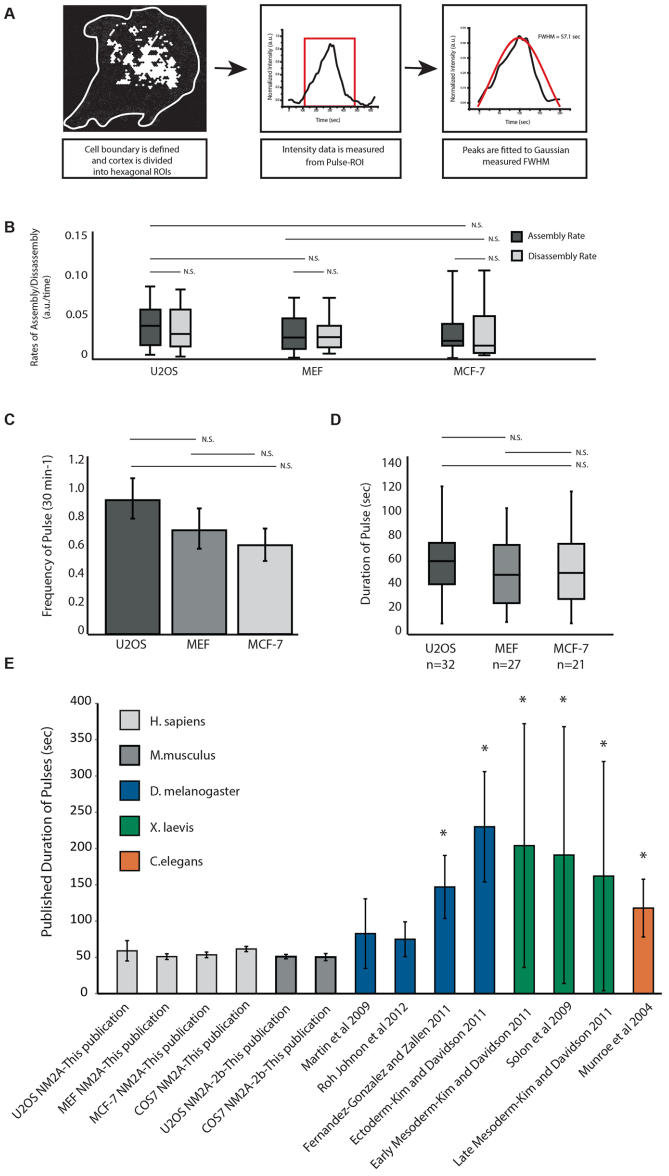

FIGURE 2: NM2A pulses occur with a similar frequency and duration in multiple cell types. (A) Pipeline for quantitative analysis of NM2A pulses in cells. Left, white hexagon ROIs are fitted based on increase in local intensity over the background; line indicates cell boundary. Center, example intensity over time plot of mEmerald-NM2A in an ROI such as that highlighted at left; red box indicates a single pulse. Right, representative intensity vs. time plot of the mEmerald-NM2A pulse (black line) fitted to a Gaussian (red line) to measure the FWHM of each peak as the pulse duration. (B–D) Thirty-minute TIRFM movies of mEmerald-NM2A were analyzed as shown in A. Rates of NM2A pulse assembly and disassembly (B), frequency (C), and duration (D) in U2OS cells (32 pulses, 36 cells), MEF (27 pulses, 39 cells), or MCF-7 cells (21 pulses, 36 cells). (E) Comparison of published NM2 pulse durations in *Drosophila melanogaster*, *Xenopus laevis*, and *C. elegans* with rates observed in this work. Color of bar indicates NM2 species. Durations and SD reported here are limited to publications that provided specific values. In B and C, significance was tested with a Student's *t* test; error for frequency is SD and for assembly, disassembly, and duration is SEM. NS, $p > 0.05$. (E) Significance was tested with one-way analysis of variance. Asterisk indicates difference is significant at $p < 0.01$, determined by post hoc Tukey test.

a significant decrease in both the pulse duration and frequency of occurrence (Figure 3, E and F, and Supplemental Movie S3). To determine whether RLC phosphorylation by a calcium-independent pathway could be required for NM2 pulsing, we inhibited Rho-associated kinase (ROCK) with Y-27632A (10 μM, 30 min) (Uehata *et al.*, 1997). Similar to the effects of MLCK inhibition, ROCK inhibition significantly reduced pulse frequency of occurrence and duration (Figure 3, E and F). Thus RLC phosphoregulation by both MLCK and ROCK is required for NM2A pulses in the cortical cytoskeleton.

We next sought to address the role of motor activity in mediating pulsed assembly and disassembly of NM2 in the cortical cytoskeleton. We used the small-molecule inhibitor blebbistatin to inhibit NM2 ATPase activity (Straight *et al.*, 2003; Limouze *et al.*, 2004). Analysis of time-lapse movies of cells expressing mApple-NM2A showed that blebbistatin treatment (30 min) caused a dose-dependent decrease in the frequency of pulse occurrence (Figure 3, G and H, and Supplemental Movie S3). However, the few pulses that did occur in cells treated with blebbistatin had a similar duration as those in control cells, suggesting that a small fraction of active NM motors may be sufficient to drive pulses at low frequency (Figure 3, G and H). Together these results indicate that local pulsed assembly and disassembly of NM2A in the cortical cytoskeleton occurs independently of integrin-ligand engagement but requires intracellular or extracellular sources of calcium, regulatory light chain phosphorylation, and motor ATPase activity.

Pulsatile dynamics are specific to NM2A

Because NM2A and NM2B isoforms exhibit differences in their mechanochemical ATPase cycle (Kovacs *et al.*, 2003; Wang *et al.*, 2003; Vicente-Manzanares *et al.*, 2009) but coassemble in cells (Kolega, 1998; Beach *et al.*, 2014; Shutova *et al.*, 2014), we sought to determine whether the NM2B isoform was capable of pulsing behavior in the cortical cytoskeleton. Expression of N-terminally tagged mEmerald-NM2B in U2OS cells showed that it incorporated into structures in the cortical cytoskeleton similarly to mEmerald-NM2A. Surprisingly, however, mEmerald-NM2B did not exhibit any pulsatile behavior but instead remained incorporated in the cytoskeleton for the duration of imaging, with no detectable transient local increases (Figure 4, A and B, and Supplemental Movie S4). To test more directly whether NM2B was capable of pulsatile behavior in cells, we used African green monkey kidney cells (COS7), which lack NM2A and express NM2B only endogenously (Tullio *et al.*, 1997; Conti *et al.*, 2004). In COS7 cells, expression of mEmerald-NM2B followed by TIRF imaging showed no apparent pulsatile behavior, whereas ectopic expression of mEmerald-NM2A induced local pulses of NM2A assembly and disassembly of similar duration but with a slightly higher frequency of occurrence than we observed with U2OS, MCF-7, and MEF cell types (Figure 4, C and D, and Supplemental Movie S4). Together these observations show that the local pulsed assembly of NM2 in the cortical cytoskeleton is specific to one or more functions of the NM2A isoform.

NM2A head domain is necessary for NM2 pulses in cortical cytoskeleton of adherent cells

We then sought to determine the molecular requirements for NM2A pulse dynamics in the cortical cytoskeleton. To test whether the head or rod and tailpiece domains conferred this function, we used two NM2 isoform chimeras previously characterized in knock-in mice (Wang *et al.*, 2011). The first chimera contains a GFP-tagged N-terminal NM2A head domain consisting of the NM2A motor and

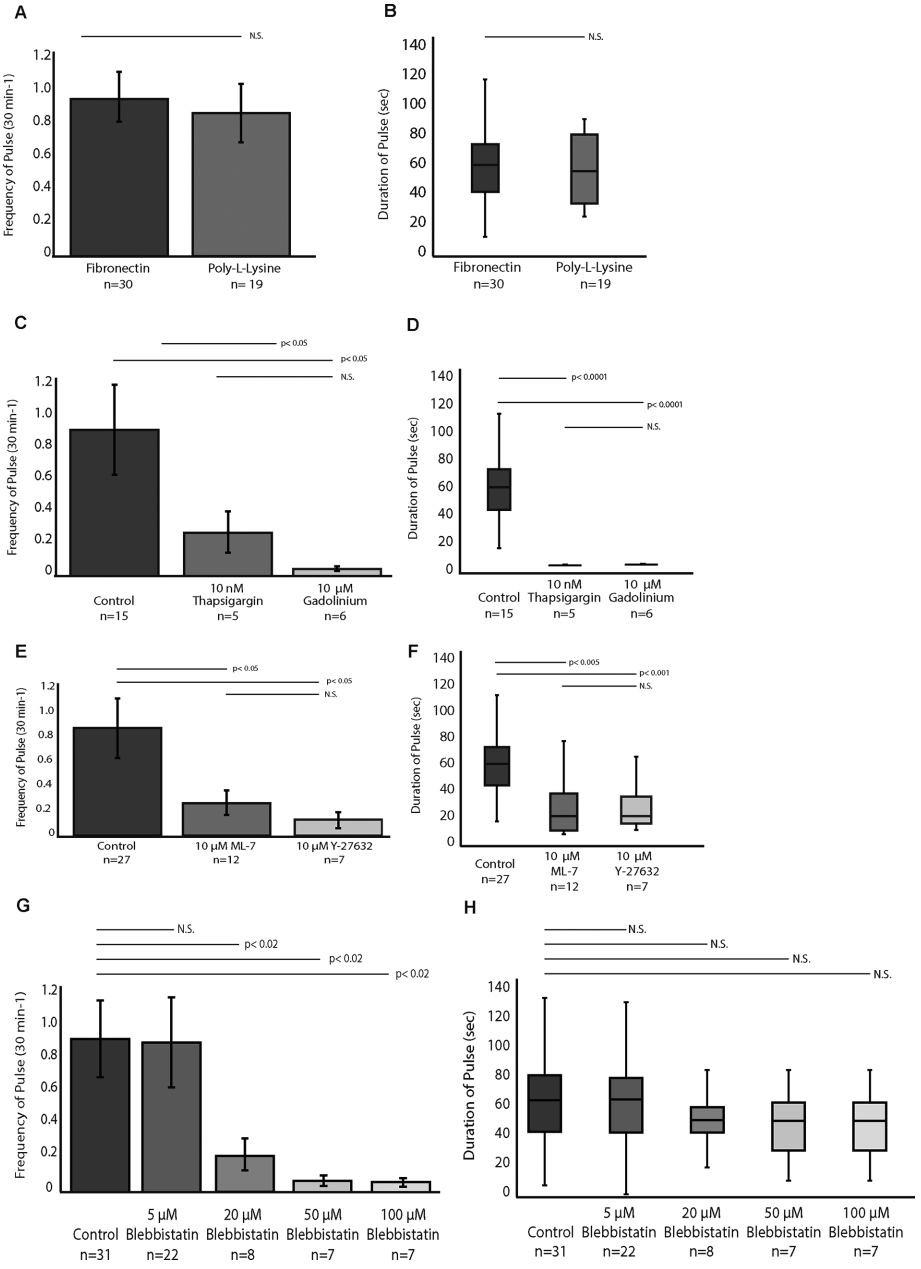

FIGURE 3: NM2A pulses are independent of integrin ligand engagement but require intracellular calcium, phosphorylation of regulatory light chains, and motor ATPase activity. U2OS cells expressing mEmerald-NM2A were plated on fibronectin-coated coverslips (unless noted otherwise), imaged for 30 min by time-lapse TIRFM, and subjected to the analysis described in Figure 2A, and pulse frequency (A, C, E, G) or pulse duration (B, D, F, H) was determined. (A, B) Comparison of cells plated on fibronectin (30 pulses from 34 cells) or poly-L-lysine (19 pulses from 23 cells). (C, D) Comparison of control cells (no treatment, 15 pulses from 17 cells), cells treated for 15 min with 10 nM thapsigargin (5 pulses from 21 cells), or cells treated for 10 min with 10 µM gadolinium (6 pulses from 20 cells). (E, F) Comparison of control cells (27 pulses from 30 cells) and cells treated for 30 min with either 10 µM ML-7 (2 pulses from 12 cells) or 10 µM Y-27632A (1 pulse from 7 cells). (G, H) Comparison of control (no treatment, 31 pulses from 35 cells) or treatment for 30 min with 5 µM (22 pulses from 25 cells), 20 µM (8 pulses from 32 cells), 50 µM (3 pulses from 35 cells), or 100 µM (3 pulses from 36 cells) blebbistatin. Significance was tested with a Student's *t* test; error for frequency is SD and for duration is SEM. NS, $p > 0.05$.

lever arm (amino acids [aa]1–836) fused in-frame to the NM2B rod and tail-piece domains (aa 844–1977), referred to as the GFP-NM2A2b chimera, and the second consisted of a GFP-tagged N-terminal NM2B head domain including the NM2B motor and lever arm (aa 1–843) fused in-frame to the NM2A rod and tail-piece domains (aa 837–1961), referred to as the GFP-NM2B2a chimera (Figure 5A).

We first verified that these chimeric molecules were capable of assembling into filaments, forming the folded and compact off-state, and were capable of mediating actin motility. The chimeric molecules were coexpressed together with RLC and the essential light chain using the baculovirus/sf9 system and purified using FLAG affinity chromatography. Actin gliding assays were used to verify that both chimeric constructs were capable of driving motility in a phosphorylation-dependent manner. As expected, after RLC phosphorylation by MLCK and in the presence of ATP, the relative gliding velocities of the chimeras were dependent on the source of the motor segment of the molecule, with the NM2A2b chimera and NM2A translocating actin filaments faster than did the NM2B2a chimera and NM2B (Figure 5B). In contrast, the unphosphorylated chimeras were incapable of driving ATP-dependent actin movement. Examination of recombinant proteins by negative-stain electron microscopy revealed that under low-salt conditions in the absence of RLC phosphorylation and ATP, both chimeras formed bipolar filaments that were nearly indistinguishable from those formed by the wild-type proteins, with the lengths of the chimeric filaments (NM2A2b = 305 [±32 nm SD; n = 75], NM2B2a = 296 [±24 nm SD; n = 45]) closely matching those previously reported for wild-type filaments under the same conditions (NM2A = 301 [±24 nm SD; n = 100], NM2B = 323 [±24 nm SD; n = 100]; Billington *et al.*, 2013). However, upon addition of ATP (0.1 mM), filaments of both chimeras disassembled into the same compact conformation described previously for wild-type NM2 molecules (Figure 5C; Billington *et al.*, 2013). This showed that the head/tail interaction sites previously demonstrated to be important in smooth and NM2 regulation are sufficiently conserved between the two NM2s to allow formation of the monomeric, enzymatically switched off-state in the absence of RLC phosphorylation. Together the results demonstrate that domains could be swapped between the two NM2 isoforms while retaining the general enzymatic and regulatory properties of the parent motor and without aberrantly affecting filament assembly.

We then examined the dynamic behavior of the chimeric NM2 molecules in cells. To prevent coassembly of the expressed chimeras with endogenous NM2A, we used small interfering RNA (siRNA)

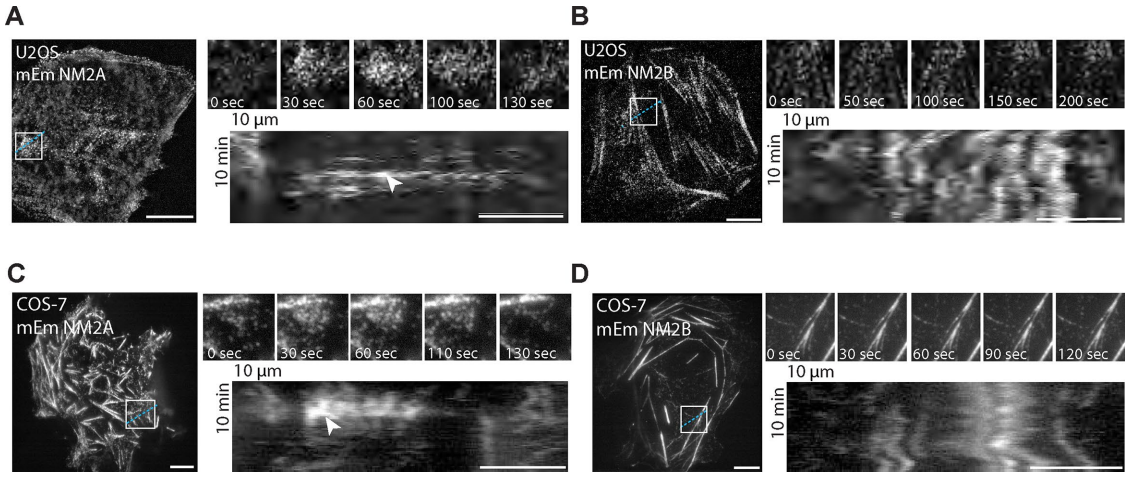

FIGURE 4: NM2 pulses are specific to NM2A. (A, B) Time-lapse TIRFM of a U2OS cell expressing either mEmerald-NM2A (A) or mEmerald-NM2B (B). Left, boxed regions highlight an individual pulse in A or a region of the cortex in B. These are shown zoomed in time-lapse image series (top right); elapsed time in seconds. Dashed blue lines (10 µm) indicate regions from which kymographs (bottom right) were taken. White arrowhead in A indicates the increase in mEmerald-NM2A fluorescence intensity during a pulse. (C, D) Time-lapse TIRFM of a COS-7 cell expressing either mEmerald-NM2A (C) or mEmerald-NM2B (D). Left, boxed regions highlight an individual pulse in C or a region of the cortex in D. These are shown zoomed in a time-lapse image series (top, right); elapsed time in seconds. Dashed blue lines (10 µm) indicate regions from which kymographs (bottom, right) were taken. White arrowhead in C indicates the increase in mEmerald-NM2A fluorescence intensity during a pulse. Scale bars, 10 µm (A–D, left), 1 µm (A–D, kymograph region).

targeted to the 3′ untranslated region to reduce NM2A protein in U20S cells by ~50–75% (Pasapera *et al.*, 2015; Figure 5D) or COS7 cells that lack endogenous NM2A. Because NM2B does not exhibit pulsing, endogenous NM2B could not contribute to pulsing of the expressed chimeras in either cell type. TIRF imaging of either of the GFP-tagged chimeras (expressed at no more that 50% over endogenous levels) in either cell system showed that both constructs correctly localized to structures in the cortical cytoskeleton (Figure 5E and Supplemental Movie S4). Analysis of time-lapse movies showed that the GFP-NM2A2b chimera displayed transient local assembly/disassembly cycles that were similar in duration and frequency to those of GFP-NM2A expressed in the same cell type (Figure 5, F and G; Supplemental Movie S4). In contrast, similar analysis of the GFP-NM2B2a chimera showed significantly lower pulse frequency and duration than with GFP-NM2A–expressing controls. Together these results demonstrate that the NM2A motor domain together with a rod and tail piece capable of forming filaments is necessary for pulsatile actomyosin dynamics in the cortical cytoskeleton of adherent cells.

We show here that transient, local assembly of NM2A, termed pulses, occurs in the cortical cytoskeleton of single adherent cells of mesenchymal, epithelial, and bone origin independently of developmental signaling cues and cell–cell or cell–ECM interactions. The role of NM2 pulsatile dynamics in generating the contractile forces in the cortical cytoskeleton that contribute to developmental morphogenesis has been characterized (Munro *et al.*, 2004; Martin *et al.*, 2009; Solon *et al.*, 2009; Badyal *et al.*, 2011; Fernandez-Gonzalez and Zallen, 2011; Roh-Johnson *et al.*, 2012; Mason *et al.*, 2013, 2016; Vasquez *et al.*, 2014; Munjal *et al.*, 2015). However, the occurrence of a similar behavior in single, isolated adherent mammalian cells has not previously been demonstrated. We find that NM2A pulsatile foci occur stochastically but with a similar frequency and duration across a range of cell types in tissue culture. Our results thus suggest that pulsatile contractions in the cortical cytoskeleton of cells are an intrinsic property of NM2A that mediates its role in homeostatic maintenance of cortical cytoskeletal tension.

We characterized the mechanisms mediating NM2A pulsing in the cortical cytoskeleton. Our results show that pulsatile foci are the result of local assembly of NM2A into the cortical cytoskeleton, and each pulse involves the assembly and disassembly of filaments in that region. Our finding that pulses in the ventral cortical cytoskeleton of single cells occur independently of integrin ligand engagement clearly differentiates them from the integrin-dependent induction of cyclic NM2 assembly in the lamellipodia of spreading (Giannone *et al.*, 2004) or migrating (Machacek *et al.*, 2009; Burnette *et al.*, 2011) cells. Our demonstration that RLC phosphorylation and cytosolic calcium are both required for NM2A assembly into pulses is not surprising, given that this phosphorylation is mediated by calcium-sensitive kinases (Hathaway and Adelstein, 1979) and is required for motor activation (Scholey *et al.*, 1980). However, it is surprising that we found that NM2 ATPase activity is required for pulsing because ATPase activity is not known to have a direct role in filament assembly. Even more surprising is the fact that pulsing specifically requires the head of NM2A, as pulsing does not occur with either NM2B or a 2B-head-2a-tail chimera. This suggests not only that NM2 ATPase activity is necessary for pulsing, but also that pulsing requires the specific properties of the NM2A motor. NM2A has been shown to be a low–duty ratio motor (Kovacs *et al.*, 2003), whereas NM2B has a higher duty ratio and dissociates more slowly after ATP hydrolysis and is thus better suited to act as a "tensile cross-linker" (Rosenfeld *et al.*, 2003; Wang *et al.*, 2003). Of importance, recent work showed that the kinetic properties of the single NM2 isoform in *Drosophila* are quite similar to those of human NM2A (Heissler *et al.*, 2015), suggesting that the kinetics required for NM2 pulsing is fundamental and conserved. In support of the importance of differences in duty ratio underlying the pulsatile behavior, replacement of the higher–duty ratio NM2B motor with the low–duty ratio NM2A motor was sufficient to induce pulsing

behavior of the resultant chimera. Thus we suggest that the kinetic differences between NM2A and NM2B motors could underlie the dichotomy in their dynamic behavior in the cortical cytoskeleton.

How could NM2A ATPase activity drive pulsatile assembly/disassembly dynamics in the cortical cytoskeleton? We speculate that the potential role for the motor activity is in the disassembly of a pulse. We found that NM2A pulse assembly is driven by recruitment of NM2A to the cortical cytoskeleton, where it can either coassemble into preexisting filaments or form new filaments. Even if these two assembly processes occur at equal rates throughout the cortical cytoskeleton, areas with denser NM2A would tend to recruit more NM2A than sparser areas because there are more preexisting filaments into which they can coassemble. This positive feedback would result in local regions of higher or lower NM2A concentration and contractility, with high-concentration regions becoming pulses. Then, because NM2 contractility drives actin disassembly in stress fibers (Wilson *et al.*, 2010; Stachowiak *et al.*, 2014) and the cytokinetic furrow (Murthy and Wadsworth, 2005), we suggest that stronger contractions in foci of high NM2A concentration could drive local disassembly of actin filaments. In this way, NM2A would drive the local destruction of its cortical cytoskeletal substrate and thus its local dissociation from the cortex, completing the cycle of a pulse. It is not known whether NM2A and NM2B differ in their ability to destroy actin filaments, but one might expect that a low–duty ratio motor that drives filament movement and buckling (Murrell and Gardel, 2012) would make a better actin destroyer than a tensile cross-linker. In addition, it has been suggested that the NM2B isoform has slower dissociation from the cortical cytoskeleton than NM2A and could be well suited to produce long-term continuous mechanical forces in the cell (Betapudi *et al.*, 2006; Beach *et al.*, 2011, 2014; Chang and Kumar, 2015), making it unable to rapidly supply subunits to distal assembling pulses. In addition, different kinases mediating NM2 RLC phosphorylation are spatially segregated in cells (Liang *et al.*, 2002), potentially playing a role in the regulation of NM2 filament assembly. Thus we do not discount the possibility that pulses may be driven by spatially and temporally local signaling cues that drive filament assembly and disassembly by phosphoregulation of the heavy chains (Dulyaninova and Bresnick, 2013; Pasapera *et al.*, 2015), calcium sparks (Lee *et al.*, 1999), or other mechanisms.

Our results, in combination with work from others, suggest that NM2 pulsatile behavior may be an intrinsic property of cortical actomyosin networks in cells. We speculate that the motor activity of NM2 on an inhomogeneous cortical actin network could result in a basal level of stochastic pulses that serve as an active homeostatic mechanism for maintaining cell tension and mechanical integrity in the cortical cytoskeleton. However, in the context of developing tissues, in which cell–cell interactions and morphogens initiate signaling cues, these stochastic pulses could become amplified and coordinated, causing the shape changes required in tissue morphogenesis.

MATERIALS AND METHODS

Reagents and plasmids

To generate the tdEos, mEmerald, and mApple NM2A vectors, tdEos-C1, mEmerald-C1, mApple-C1, and GFP-NM2A were digested with *Nhe*I and *Age*I and ligated to form tdEos-NM2A-C-18, mEmerald-NM2A-C-18, and mApple-NM2A-C-18 vectors. The mApple CAAX plasmid was generated by digesting mApple-N1 and mEmerald-CAAX with *Age*I and *Bsp*EI, gel purified, and ligated to form mApple-CAAX. The mApple F-Tractin plasmid was generated as previously described (Li *et al.*, 2015). To generate the mEmerald NM2B expression vector, human NM2B cDNA (NM_005964.1) was PCR amplified with a 5′ primer encoding a *Bsp*EI site and a 3′ primer encoding a *Kpn*I site. The PCR products were then digested, gel purified, and ligated with an mEmerald-C1 cloning vector to generate mEmerald-NM2B-C-18. To generate the NM2 chimeras, GFP-NM2A2b consisted of amino acids 1–836 of NM2A and 844–1977 of NM2B, and GFP-NM2B2a consisted of amino acids 1–843 of NM2B and 837–1961 of NM2A. cDNAs encoding human chimeric nonmuscle NM2 heavy chains (NM2A2b/NM2B2a) were amplified by PCR using plasmid DNA templates described previously (Wang *et al.*, 2010) and cloned into the baculovirus transfer vector pFastBac1, which was modified to incorporate nucleotides encoding a FLAG tag epitope (DYKDDDDK) at the N-terminal for purification and the appropriate restriction sites for cloning (Billington *et al.*, 2013). The primers used to amplify NM2A2b and NM2B2a were 5′-ATAAGAATGCGGCCGCGATGGCACAGCAAGCTGCCGAT-3′ and 5′-GGGGTACCTTACTCTGACTGGGGTGGCTG-3′ for 2AB and 5′-ATAAGAATGCGGCCGCGATGGCGCAGAGAACTGGACTC-3′ and 5′-GGGGTACCTTATTCGGCAGGTTTGGCCTC-3′ for 2BA. *Not*I and *Kpn*I restriction sites marked by underlines were incorporated into the forward and reverse primers, respectively. All DNA used for transfection was prepared and purified using the Plasmid Maxi kit (Qiagen, Valencia, CA) according to manufacturer's instructions.

Cell culture and transient transfection

U2OS cells were obtained from the American Type Culture Collection (Manassas, VA) and maintained at 37°C in McCoy's 5A medium (Invitrogen, Carlsbad, CA) supplemented with 10% fetal bovine serum (FBS; Life Technologies, Carlsbad, CA) at 5% CO_2. MCF-7 and COS-7 cells were obtained from the American Type Culture Collection and maintained at 37°C in DMEM (Life Technologies) supplemented with 10% FBS at 5% CO_2. Primary MEFs were isolated as follows. Animals were maintained according to guidelines approved by National Heart, Lung and Blood Institute Institutional Animal Care and Use Committee. Mice were kept on a C57J/BL6 background. Embryonic day 13.5 embryos obtained from timed matings were dissected from pregnant females and decapitated before internal organs were removed. Remaining tissue was cut into pieces and incubated 3 × 10 min in 0.25 mg/ml trypsin/EDTA (Life Technologies). After digestion, the pooled suspensions were passed through 100-µm nylon mesh, and cells were pelleted (5 min, 200 × *g*) and plated. Nonadherent cells were removed after 2 h, and cultures were maintained in DMEM supplemented with 20% FBS at 5% CO_2. MEFs were used for experiments at passages 2–4. Transfections were performed using a Nucleofector (U2OS: solution V, program X-001; COS-7: solution V, program A-024; MCF-7: solution V, program P-020; MEF: solution V, program T-020; Lonza, Basel, Switzerland). Expression of endogenous NM2A was knocked down by siRNA as previously described (Pasapera *et al.*, 2015). Briefly, we used the Accel siRNA Delivery protocol and a 3′ untranslated region siRNA sequence from Thermo Scientific (A-007668-13-0020 Accell Human MYH9 siRNA). Accell siRNA solution was added at a final concentration of 1 mM siRNA MYH9. Cells were incubated with siRNA for 48 h and then transfected with the respective expression vectors for GFP-NM2A chimeras. Live-cell imaging was performed in growth medium without phenol red and supplemented with 25 mM 4-(2-hydroxyethyl)-1-piperazineethanesulfonic acid, pH 7.2, and 30 U/ml Oxyrase (Oxyrase, Mansfield, OH). For experiments, cells were plated for 16–20 h before imaging on 22 × 22 mm #1.5 coverslips coated with 10 µg/ml fibronectin (1 h at 37°C; Millipore, Billerica, MA), mounted on a slide with ~30 µl of

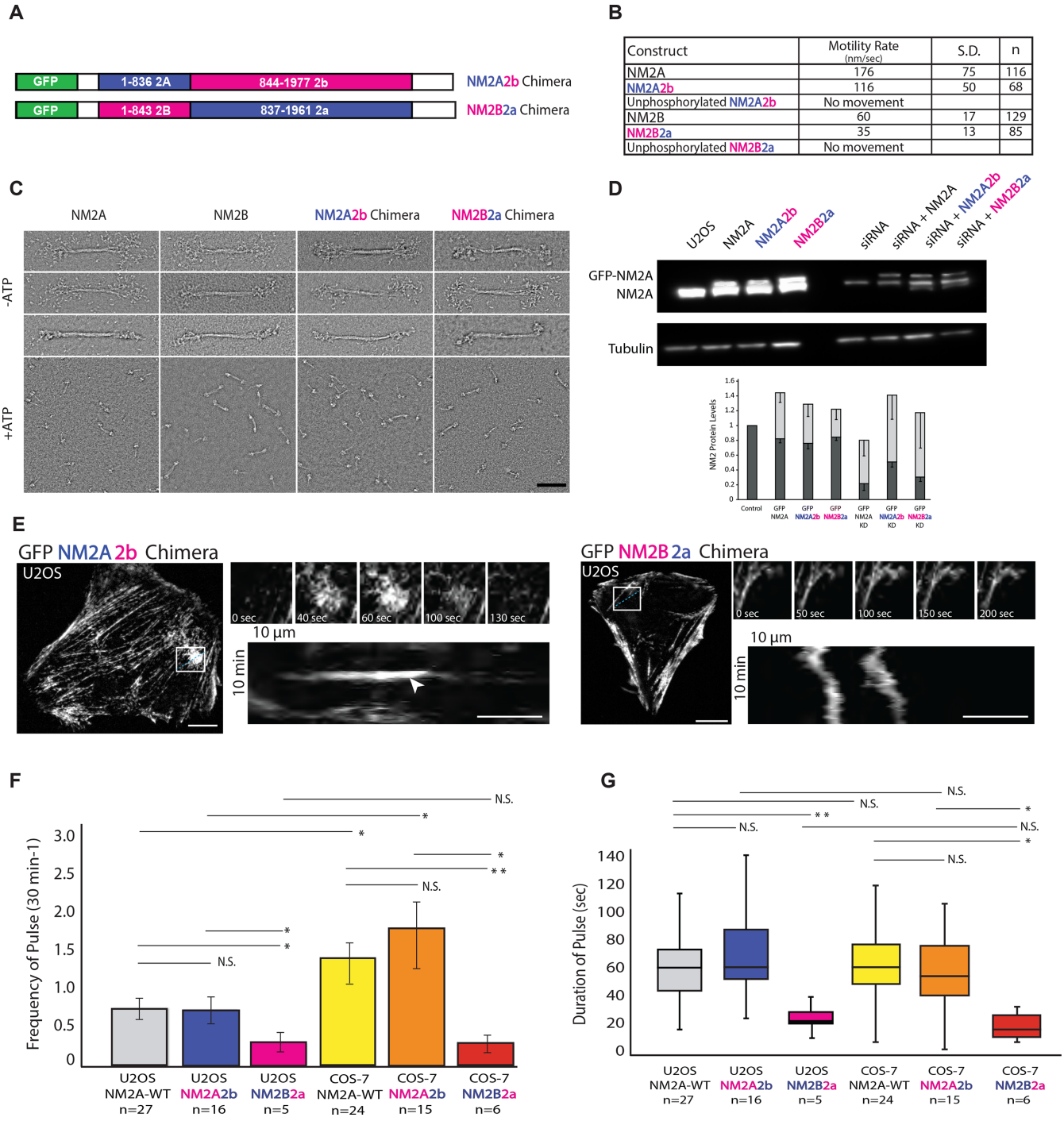

FIGURE 5: NM2 pulses require the NM2A motor domain. (A) Schematic representation of GFP-NM2A2b and GFP-NM2B2a chimera constructs. Green, white, blue, and pink represent GFP, linker, NM2A, and NM2B sequences, respectively; amino acid positions in the respective NM2 sequences are noted by the numbers. (B) Purified NM2 isoforms or chimeras were phosphorylated by MLCK, and the motility of fluorescent actin in the presence of ATP was assayed by TIRFM. Velocities of actin movement were measured from time-lapse movies. (C) Negative-stain electron microscopy images of purified NM2A (column 1), NM2B (column 2), NM2A2b (column 3), and NM2B2a (column 4). Top three rows are examples of bipolar NM2 filaments obtained in the absence of ATP. Bottom row is an example field of view showing unphosphorylated NM2 in the presence of 0.1 mM ATP. Scale bar, 100 nm. (D) Western blot (top) and quantification (bottom) of U2OS cells treated with siRNAs targeted to the 3′ untranslated region of NM2A (siRNA NM2A) and expression of GFP-NM2 constructs. Blots were probed with antibodies to GFP, NM2A, and tubulin. Bottom, quantification of endogenous (dark gray) and ectopically expressed NM2 constructs (light gray), each normalized to individual tubulin loading control and then normalized to the endogenous NM2A level in untransfected control. Error is SEM (three experiments). (E) Time-lapse TIRFM of U2OS cells in which NM2A was knocked down by siRNA and the cells reexpressed either GFP-NM2A2b or GFP-NM2B2a chimera constructs. Left, boxed regions highlight an individual pulse in (GFP-NM2A2b) or a region of the cortex in (GFP-NM2B2a). These are shown zoomed in time-lapse image series

imaging medium, and sealed with Valap. Perfusion experiments were performed with #1.5, 35-mm glass-bottom dishes (MatTek, Ashland, MA) coated with 10 µg/ml fibronectin (1 h at 37°C; Millipore). To block integrin engagement, cells were plated for 12–15 h before imaging on 22 × 22 mm #1.5 coverslips coated with 10 µg/ml poly-L-lysine (1 min at 37°C; Sigma-Aldrich, St. Louis, MO).

Pharmacological treatments

The following pharmacological inhibitors were used: 5–100 µM blebbistatin (30 min; Toronto Research Chemicals, North York, Canada), Y-27632 (30 min, 10 µM; Calbiochem, Gibbstown, NJ), ML-7 (30 min, 10 µM; Calbiochem), gadolinium (10 min, 10 µM; Sigma-Aldrich), and thapsigargin (15 min, 10 nM; Sigma-Aldrich).

Western blot

Cell lysates were prepared with 2× Laemmli sample buffer and separated by SDS–PAGE, transferred to Immobilon-P membrane (Millipore), and blocked with 5% nonfat dry milk in TBS-T buffer (20 mM Tris, pH 7.6, 137 mM $NaCl_2$, 0.1% Tween-20). Membranes were incubated with primary antibodies overnight at 4°C, washed with TBS-T, incubated with the relevant horseradish peroxidase–conjugated secondary antibody, and visualized via chemiluminescence (GE Healthcare, Piscataway, NJ). Antibodies used were rabbit anti-NM2A (1:3000; Covance, Emeryville, CA), mouse anti-tubulin (1:4000; DM1A; Sigma-Aldrich), and mouse anti-GFP (1:4000; Sigma-Aldrich).

Light microscopy

Time-lapse fluorescence microscopy of EGFP-, mEmerald-, and mApple-tagged proteins in living cells was performed at 37°C using an Apo TIRF 100×/1.49 numerical aperture (NA) oil immersion objective lens (for TIRF imaging; Nikon Instruments, Melville, NY) or a Plan Apo 100×/1.40 NA Ph oil immersion objective lens (for photoconversion and confocal imaging; Nikon) on an inverted TE2000E2 microscope system (Nikon; Shin *et al.*, 2010). Illumination was provided by a custom laser combiner (Spectral Applied Research, Canada) containing solid-state 488-nm (100 mW), 561-nm (550 mW), and 405-nm (100 mW) lasers delivered via single-mode optical fibers (Oz Optics, Canada) to an automated TIRF illuminator (Nikon) or to a spinning-disk confocal scan head (Yokogawa, Mitaka, Japan). For photoconversion experiments, a galvanometric mirror system scanned a user-defined region of interest (ROI) in the image plane (FRAPPA, Andor Technology, Belfast, United Kingdom). A 10-s pulse of the 405-nm laser at 60% power within the ROI was used to photoconvert tdEos from green to red. After photoconversion, pairs of spinning-disk confocal images were acquired as fast as possible using the 488- and 561-nm lasers to track the redistribution of NM2A. All TIRF imaging was performed with an evanescent field depth of ~100 nm using a multibandpass dichromatic mirror (Chroma Technology, Bellows Falls, VT) and single-bandpass emission filters (Chroma Technology) mounted in an electronic filter wheel. Specimen positioning was achieved with a servomotor-controlled stage (Applied Scientific Instruments, Eugene, OR) equipped with a piezo top plate (Applied Scientific Instruments), and focus was controlled using the Perfect Focus System (Nikon). Temperature was maintained at 37°C using an airstream incubator (NevTek, Williamsville, VA). Pairs of EGFP (using 488-nm laser illumination) and mApple (using 561-nm laser illumination) images were captured in rapid succession at 10-s intervals using either a cooled charge-coupled (CCD) device camera operated in the 14-bit mode (for TIRF imaging; CoolSNAP HQ2; Photometrics), a cooled complementary metal-oxide semiconductor (CMOS) camera (for TIRF imaging, Myo; Photometrics), or an electron-multiplying CCD operated in the 5-MHz readout mode using electron-multiplying gain (for photoconversion and confocal imaging, Cascade II:1024; Photometrics). For light microscopy image analysis, all movies were ended after a standard duration of 30 min to minimize deleterious effects from photobleaching. Image acquisition and microscope control were achieved using MetaMorph software (MDS Analytical Technologies, Downingtown, PA).

Image analysis

All images were first background corrected using the rolling ball background subtraction plug-in from ImageJ (National Institutes of Health, Bethesda, MD), where a local background value is determined per pixel by averaging the intensity values over a radius of the 50 pixels surrounding, and subtracting from the original value. The image series was also corrected for photobleaching using the ImageJ plug-in for bleach correction based on a fit of the integrated intensity of each frame of the series over time to a single-exponential decay (wiki.cmci.info/downloads/bleach_corrector). To define a pulse region of local NM2 accumulation in the cortical cytoskeleton, a customizable ImageJ plug-in was obtained from Lance Davidson (Kim and Davidson, 2011) and used to identify areas of the cell that exhibited transient fluctuations of NM2 intensity changes within defined parameters to avoid any experimental bias. In brief, a ROI was hand drawn around the periphery of each individual cell to delineate the cell boundary. The "cell-ROI" was then automatically segmented into small hexagonal units termed "hexagonal-ROIs" to create thousands of individual regions. After segmentation, each hexagonal-ROI with a local fluorescence intensity change of at least 1.2 times over the background intensity level and that persisted more than three frames was saved. Each connected grouping of hexagonal-ROI units that all exhibited such change was categorized as a pulse region and segmented out to form a "pulse-ROI." The total intensity in these pulse-ROIs were tracked over time and normalized to the maximum intensity in the series. The increase and subsequent decrease in intensity for each pulse were then fitted to a Gaussian model (OriginPro; OriginLab, Northampton, MA), and only data with an r^2 of the Gaussian fit >0.9 was used for subsequent analysis. The duration of a pulse was defined as the full-width at

(top right); elapsed time in seconds. Dashed blue lines (10 µm) indicate regions from which kymographs (bottom right) were taken. White arrowhead indicates the increase in fluorescence intensity during a pulse. (F, G) U2OS cells expressing mEmerald-NM2A or cells in which NM2A was knocked down by siRNA and the cells reexpressed either GFP-NM2A2b or GFP-NM2B2a chimera constructs, or COS7 cells expressed mEmerald-NM2A, GFP-NM2A2b, or GFP-NM2B2a, were plated on fibronectin-coated coverslips, imaged for 30 min by time-lapse TIRFM, and subjected to the analysis described in Figure 2A. Pulse frequency (F) and pulse duration (G) were determined. mEmerald-NM2A (U2OS: 27 pulses from 28 cells; COS7: 39 pulses from 24 cells), GFP-NM2A2b Chimera (U2OS: 16 pulses from 18 cells; COS7: 31 pulses from 15 cells) and NM2B2a Chimera (U2OS: five pulses from 14 cells; COS7: three pulses from 10 cells). Error for frequency is SD and for duration is SEM. NS, $p > 0.05$. *$p < 0.05$, **$p < 0.01$. Scale bars, 10 µm (E, F, left), 1 µm (E, F, kymograph region), 100 nm (C).

half-maximal intensity of the Gaussian model. Owing to the stochastic nature of the pulses, frequency was determined by counting the number of pulses identified by the plug-in during each 30-min time-lapse movie. The SD of the average pulse frequency was determined as the frequency of pulses divided by the square root of the number of pulses, as previously described (Walker *et al.*, 1988). Fourier and power spectral analysis was performed using fast Fourier transform (FFT) analysis (OriginPro). Kymograph analysis was performed using MetaMorph. Statistical significance between groups was determined using two-tailed Student's *t* test assuming unequal variance. $p \leq 0.05$ was considered significant.

Actin gliding assay

The expression and purification of these two full-length chimeric NM2 proteins were carried out as previously described (Billington *et al.*, 2013). The motility assay was performed as previously described, with some modifications when measuring the activity of full-length NMs (Sellers, 2001). Briefly, monomeric NM2A, NM2B, NM2A2b, or NM2B2a full-length molecules at 1 μM concentration in high-salt buffer (0.5 M KCl, 10 mM 3-(*N*-morpholino)propanesulfonic acid [MOPS], pH 7.0, 0.1 mM ethylene glycol tetraacetic acid [EGTA], 1 mM dithiothreitol [DTT]) were applied to a 10-μl flow cell containing a nitrocellulose-coated coverslip and allowed to adhere for 1 min. The NM was removed from the flow cell, and the remaining surfaces were coated by washing the flow cell with 1 mg/ml bovine serum albumin in high-salt buffer. The flow cell was then washed with AB buffer (50 mM KCl, 20 mM MOPS, pH 7.4, 0.1 mM EGTA, 4 mM $MgCl_2$, 1 mM ATP) containing 2 μM F-actin and allowed to incubate for 5 min. For experiments in which the NM was to be phosphorylated, 0.2 mM $CaCl_2$, 1 nM myosin light chain kinase, and 0.1 μM calmodulin were included in the buffer. This wash allowed inactive NM motor domains to be tightly bound to unlabeled F-actin, thus eliminating their subsequent effect in the motility assay, and, when the calcium, myosin light chain kinase, and calmodulin were included, phosphorylated the RLC. The excess unlabeled actin was removed by washing with AB buffer, and 10 nM rhodamine-phalloidin–labeled actin in AB was added and incubated for 10–15 s. Motility was initiated by the addition of AB buffer containing 1 mM ATP and 50 mM DTT, 2.5 mg/ml glucose, 25 μg/ml glucose oxidase, and 45 μg/ml catalase to scavenge oxygen. The temperature of the flow cell was maintained at 30°C via an objective lens heater. Data were recorded and quantified as previously described (Homsher *et al.*, 1992).

Electron microscopy

NM was diluted to a concentration of 100 nM in 10 mM MOPS, pH 7.0, 0.1 mM EGTA, 2 mM $MgCl_2$, and 150 mM KCl supplemented with 0.1 mM MgATP where indicated. For NM imaged in the presence of ATP, the protein was cross-linked for 1 min at room temperature by adding glutaraldehyde to a final concentration of 0.1%. The reaction was quenched by adding Tris-HCl, pH 8.0, to a final concentration of 100 mM. A 5-μl drop of sample was applied to a carbon-coated copper grid (pretreated with ultraviolet light) and stained with 1% uranyl acetate. Micrographs were recorded on a JEOL 1200EX II microscope operating at room temperature. Data were recorded on an AMT XR-60 CCD camera. Catalase crystals were used as a size calibration standard. Measurements were carried out using ImageJ software. Contour lengths were measured using a freehand line, and a spline was fitted to reduce interpolation error. Individual images in the figures are displayed after application of the ImageJ FFT bandpass filter operation (between 40 and 3 pixels) and contrast scaled after filtering to allow easier visualization.

ACKNOWLEDGMENTS

We thank the Hammer lab at the National Heart, Lung and Blood Institute for helpful discussion and reagents; Hye Kim, Callie Miller, and Lance Davidson's lab at the University of Pittsburgh for software and discussion; Mike Davidson at Florida State University for reagents; Colleen Skau for assistance with MEF preparations; William Shin for work on the Waterman Lab microscopes; and Schwanna Thacker for administrative assistance. We thank the Electron Microscopy Core Facility of the National Heart, Lung and Blood Institute for support, advice, and use of facilities. This work was supported by the Intramural Program of the National Heart, Lung and Blood Institute, National Institutes of Health, Bethesda, MD.

REFERENCES

Badyal SK, Basran J, Bhanji N, Kim JH, Chavda AP, Jung HS, Craig R, Elliott PR, Irvine AF, Barsukov IL, *et al.* (2011). Mechanism of the Ca 2+-dependent Interaction between S100A4 and tail fragments of nonmuscle myosin heavy chain IIA. J Mol Biol 405, 1004–1026.

Barr FA, Gruneberg U (2007). Cytokinesis: placing and making the final cut. Cell 131, 847–860.

Beach JR, Hussey GS, Miller TE, Chaudhury A, Patel P, Monslow J, Zheng Q, Keri RA, Reizes O, Bresnick AR, *et al.* (2011). Myosin II isoform switching mediates invasiveness after TGF-β-induced epithelial-mesenchymal transition. Proc Natl Acad Sci USA 108, 17991–17996.

Beach JR, Shao L, Remmert K, Li D, Betzig E, Hammer J (2014). Nonmuscle myosin II isoforms coassemble in living cells. Curr Biol 24, 1160–1166.

Bertet C, Sulak L, Lecuit T (2004). Myosin-dependent junction remodelling controls planar cell intercalation and axis elongation. Nature 429, 667–671.

Betapudi V, Licate LS, Egelhoff TT (2006). Distinct roles of nonmuscle myosin II isoforms in the regulation of MDA-MB-231 breast cancer cell spreading and migration. Cancer Res 66, 4725–4733.

Billington N, Wang A, Mao J, Adelstein RS, Sellers JR (2013). Characterization of three full-length human nonmuscle myosin II paralogs. J Biol Chem 288, 33398–33410.

Blanchard GB, Murugesu S, Adams RJ, Martinez-Arias A, Gorfinkiel N (2010). Cytoskeletal dynamics and supracellular organisation of cell shape fluctuations during dorsal closure. Development 137, 2743–2752.

Booth C, Koch GL (1989). Perturbation of cellular calcium induces secretion of luminal ER proteins. Cell 59, 729–737.

Bresnick AR (1999). Molecular mechanisms of nonmuscle myosin-II regulation. Curr Opin Cell Biol 11, 26–33.

Burnette DT, Manley S, Sengupta P, Sougrat R, Davidson MW, Kachar B, Lippincott-Schwartz J (2011). A role for actin arcs in the leading-edge advance of migrating cells. Nat Cell Biol 13, 371–382.

Burnette DT, Shao L, Ott C, Pasapera AM, Fischer RS, Baird MA, Der Loughian C, Delanoe-Ayari H, Paszek MJ, Davidson MW, *et al.* (2014). A contractile and counterbalancing adhesion system controls the 3D shape of crawling cells. J Cell Biol 205, 83–96.

Chang C-W, Kumar S (2015). Differential contributions of nonmuscle myosin II isoforms and functional domains to stress fiber mechanics. Sci Rep 5, 13736.

Conti MA, Even-Ram‫ן‬ S, Liu C, Yamada KM, Adelstein RS (2004). Defects in cell adhesion and the visceral endoderm following ablation of nonmuscle myosin heavy chain II-A in mice. J Biol Chem 279, 41263–41266.

Dulyaninova NG, Bresnick AR (2013). The heavy chain has its day: regulation of myosin-II assembly. Bioarchitecture 3, 1.

Fernandez-Gonzalez R, Zallen JA (2011). Oscillatory behaviors and hierarchical assembly of contractile structures in intercalating cells. Phys Biol 8, 45005.

Giannone G, Dubin-Thaler BJ, Dobereiner H-G, Kieffer N, Bresnick AR, Sheetz MP (2004). Periodic lamellipodial contractions correlate with rearward actin waves. Cell 116, 431–443.

Hathaway DR, Adelstein RS (1979). Human platelet myosin light chain kinase requires the calcium-binding protein calmodulin for activity. Proc Natl Acad Sci USA 76, 1653–1657.

He L, Wang X, Tang HL, Montell DJ (2010). Tissue elongation requires oscillating contractions of a basal actomyosin network. Nat Cell Biol 12, 1133–1142.

Heissler SM, Chinthalapudi K, Sellers JR (2015). Kinetic characterization of the sole nonmuscle myosin-2 from the model organism Drosophila melanogaster. FASEB J 29, 1456–1466.

Homsher E, Wang F, Sellers JR (1992). Factors affecting movement of F-actin filaments propelled by skeletal muscle heavy meromyosin. Am J Physiol 262, C714–C723.
Kim HY, Davidson LA (2011). Punctuated actin contractions during convergent extension and their permissive regulation by the noncanonical Wnt-signaling pathway. J Cell Sci 124, 635–646.
Klemke RL, Cai S, Giannini AL, Gallagher PJ, de Lanerolle P, Cheresh DA (1998). Regulation of cell motility by mitogen-activated protein kinase. J Cell Biol 137, 481–492.
Kolega J (1998). Cytoplasmic dynamics of myosin IIA and IIB: spatial "sorting" of isoforms in locomoting cells. J Cell Sci 111, 2085–2095.
Koride S, He L, Xiong L-P, Lan G, Montell DJ, Sun SX, Edelstein-keshet L, Sean X, Sun SX (2014). Mechanochemical regulation of oscillatory follicle cell dynamics in the developing Drosophila egg chamber. Mol Biol Cell 25, 3709–3716.
Kovacs M, Wang F, Hu A, Zhang Y, Sellers JR (2003). Functional divergence of human cytoplasmic myosin II. Kinetic characterization of the non-muscle IIA isoform. J Biol Chem 278, 38132–38140.
Lecuit T, Lenne P-F (2007). Cell surface mechanics and the control of cell shape, tissue patterns and morphogenesis. Nat Rev Mol Cell Biol 8, 633–644.
Lee J, Ishihara A, Oxford G, Johnson B, Jacobson K (1999). Regulation of cell movement is mediated by stretch-activated calcium channels. Nature 400, 382–386.
Li D, Shao L, Chen B-C, Zhang X, Zhang M, Moses B, Milkie DE, Beach JR, Hammer JA, Pasham M, *et al*. (2015). Extended-resolution structured illumination imaging of endocytic and cytoskeletal dynamics. Science, 349.
Liang W, Licate LS, Warrick HM, Spudich JA, Egelhoff TT (2002). Differential localization in cells of myosin II heavy chain kinases during cytokinesis and polarized migration. BMC Cell Biol 3, 1–16.
Limouze J, Straight AF, Mitchison T, Sellers JR (2004). Specificity of blebbistatin, an inhibitor of myosin II. J Muscle Res Cell Motil 25, 337–341.
Machacek M, Hodgson L, Welch C, Elliott H, Pertz O, Nalbant P, Abell A, Johnson GL, Hahn KM, Danuser G (2009). Coordination of Rho GTPase activities during cell protrusion. Nature 461, 99–103.
Martin AC, Kaschube M, Wieschaus EF (2009). Pulsed contractions of an actin. myosin network drive apical constriction. Nature 457, 495.
Mason FM, Martin AC (2011). Tuning cell shape change with contractile ratchets. Curr Opin Genet Dev 21, 671–679.
Mason FM, Tworoger M, Martin AC (2013). Apical domain polarization localizes actin-myosin activity to drive ratchet-like apical constriction. Nat Cell Biol 15, 926–936.
Mason FM, Xie S, Vasquez CG, Tworoger M, Martin AC (2016). RhoA GTPase inhibition organizes contraction during epithelial morphogenesis. J Cell Biol 214, 603–617.
Munjal A, Philippe J-M, Munro E, Lecuit T (2015). A self-organized biomechanical network drives shape changes during tissue morphogenesis. Nature 524, 351–355.
Munro E, Nance J, Priess JR (2004). Cortical flows powered by asymmetrical contraction transport PAR proteins to establish and maintain anterior-posterior polarity in the early C. elegans embryo. Dev Cell 7, 413–424.
Murrell MP, Gardel ML (2012). F-actin buckling coordinates contractility and severing in a biomimetic actomyosin cortex. Proc Natl Acad Sci USA 109, 20820–20825.
Murthy K, Wadsworth P (2005). Myosin-II-dependent localization and dynamics of F-actin during cytokinesis. Curr Biol 15, 724–731.
Pasapera AM, Plotnikov SV, Fischer RS, Case LB, Egelhoff TT, Waterman CM (2015). Rac1-dependent phosphorylation and focal adhesion recruitment of myosin IIA regulates migration and mechanosensing. Curr Biol 25, 175–186.
Polte TR, Eichler GS, Wang N, Ingber DE (2004). Extracellular matrix controls myosin light chain phosphorylation and cell contractility through modulation of cell shape and cytoskeletal prestress. Am J Physiol Cell Physiol 286, C518–C528.
Rauzi M, Lenne P-F, Lecuit T (2010). Planar polarized actomyosin contractile flows control epithelial junction remodelling. Nature 468, 1110–1114.
Roh-Johnson M, Shemer G, Higgins CD, McClellan JH, Werts AD, Tulu US, Gao L, Betzig E, Kiehart DP, Goldstein B (2012). Triggering a cell shape change by exploiting preexisting actomyosin contractions. Science 335, 1232–1235.
Rosenfeld SS, Xing J, Chen LQ, Sweeney HL (2003). Myosin IIB is unconventionally conventional. J Biol Chem 278, 27449–27455.
Saitoh M, Ishikawa T, Matsushima S, Naka M, Hidaka H (1987). Selective inhibition of catalytic activity of smooth muscle myosin light chain kinase. J Biol Chem 262, 7796–7801.
Scholey JM, Taylor KA, Kendrick-Jones J (1980). Regulation of nonmuscle myosin assembly by calmodulin-dependent light chain kinase. Nature 287, 233–235.
Sellers JR (2001). In vitro motility assay to study translocation of actin by myosin. Curr Protoc Cell Biol Chapter 13, Unit 13.2.
Shin W, Fischer RS, Kanchanawong P, Kim Y, Meyers KA, Nishimura Y, Plotnick SV, Thievessen I, Yarar D (2010). A Versatile, Multi-Color Total Internal Reflection Fluorescence and Spinning Disk Confocal Microscope System for High-Resolution Live Cell Imaging, Cold Spring Harbor, NY: Cold Spring Harbor Laboratory Press.
Shutova MS, Spessott WA, Giraudo CG, Svitkina T (2014). Endogenous species of mammalian nonmuscle myosin IIA and IIB include activated monomers and heteropolymers. Curr Biol 24, 1958–1968.
Skoglund P, Rolo A, Chen X, Gumbiner BM, Keller R (2008). Convergence and extension at gastrulation require a myosin IIB-dependent cortical actin network. Development 135, 2435–2444.
Sokolow A, Toyama Y, Kiehart DP, Edwards GS (2012). Cell ingression and apical shape oscillations during dorsal closure in Drosophila. Biophys J 102, 969–979.
Solon J, Kaya-Copur A, Colombelli J, Brunner D (2009). Pulsed forces timed by a ratchet-like mechanism drive directed tissue movement during dorsal closure. Cell 137, 1331–1342.
Stachowiak MR, Smith MA, Blankman E, Chapin LM, Balcioglu HE, Wang S, Beckerle MC, O'Shaughnessy B (2014). A mechanical-biochemical feedback loop regulates remodeling in the actin cytoskeleton. Proc Natl Acad Sci USA 111, 17528–17533.
Straight AF, Cheung A, Limouze J, Chen I, Westwood NJ, Sellers JR, Mitchison TJ (2003). Dissecting temporal and spatial control of cytokinesis with a myosin II Inhibitor. Science 299, 1743–1747.
Tullio AN, Accili D, Ferrans VJ, Yu ZX, Takeda K, Grinberg A, Westphal H, Preston YA, Adelstein RS (1997). Nonmuscle myosin II-B is required for normal development of the mouse heart. Proc Natl Acad Sci USA 94, 12407–12412.
Uehata M, Ishizaki T, Satoh H, Ono T, Kawahara T, Morishita T, Tamakawa H, Yamagami K, Inui J, Maekawa M, *et al*. (1997). Calcium sensitization of smooth muscle mediated by a Rho-associated protein kinase in hypertension. Nature 389, 990–994.
Vasquez CG, Tworoger M, Martin AC (2014). Dynamic myosin phosphorylation regulates contractile pulses and tissue integrity during epithelial morphogenesis. J Cell Biol 206, 435–450.
Vicente-Manzanares M, Koach MA, Whitmore L, Lamers ML, Horwitz AF (2008). Segregation and activation of myosin IIB creates a rear in migrating cells. J Cell Biol 183, 543–554.
Vicente-Manzanares M, Ma X, Adelstein RS, Horwitz AR (2009). Non-muscle myosin II takes centre stage in cell adhesion and migration. Nat Rev Mol Cell Biol 10, 778–790.
Walker RA, O'Brien ET, Pryer NK, Soboeiro MF, Voter WA, Erickson HP, Salmon ED (1988). Dynamic instability of individual microtubules analyzed by video light microscopy: rate constants and transition frequencies. J Cell Biol 107, 1437–1448.
Wang A, Ma X, Conti MA, Adelstein RS (2011). Distinct and redundant roles of the nonmuscle myosin II isoforms and functional domains. Biochem Soc Trans 39, 1131–1135.
Wang A, Ma X, Conti MA, Liu C, Kawamoto S, Adelstein RS (2010). Nonmuscle myosin II isoform and domain specificity during early mouse development. Proc Natl Acad Sci USA 107, 14645–14650.
Wang F, Kovacs M, Hu A, Limouze J, Harvey EV, Sellers JR (2003). Kinetic mechanism of nonmuscle myosin IIB. Functional adaptations for tension generation and maintenance. J Biol Chem 278, 27439–27448.
Wilson CA, Tsuchida MA, Allen GM, Barnhart EL, Applegate KT, Yam PT, Ji L, Keren K, Danuser G, Theriot JA (2010). Myosin II contributes to cell-scale actin network treadmilling through network disassembly. Nature 465, 373–377.
Yang XC, Sachs F (1989). Block of stretch-activated ion channels in Xenopus oocytes by gadolinium and calcium ions. Science 243, 1068–1071.
Zhou M, Wang Y-L (2008). Distinct pathways for the early recruitment of myosin II and actin to the cytokinetic furrow. Mol Biol Cell 19, 318–326.